

Hard-photon production with b jets at hadron colliders

H. B. Hartanto^{1,2,*} and L. Reina^{2,†}

¹*Insitut für Theoretische Teilchenphysik und Kosmologie,*

RWTH Aachen University, D-52056 Aachen, Germany

²*Physics Department, Florida State University, Tallahassee, FL 32306-4350, USA*

(Dated: October 18, 2018)

Abstract

We present total and differential cross sections for the production of a hard photon with up to two b jets at both the Tevatron with center-of-mass energy 1.96 TeV and the Large Hadron Collider with center-of-mass energy 8 TeV, including Next-to-Leading Order (NLO) QCD corrections and full b -quark mass effects. We study the theoretical uncertainty due to the residual renormalization- and factorization-scale dependence and explain its origin on the basis of the different subprocesses contributing to the NLO cross section. We specifically address the case of the production of a hard photon with at least one b jet and compare the NLO QCD predictions in both the Four- and Five-Flavor-Number Schemes to the experimental measurements obtained by CDF and D0.

*Electronic address: hartanto@physik.rwth-aachen.de

†Electronic address: reina@hep.fsu.edu

I. INTRODUCTION

The associated production of a hard photon with a heavy-quark pair ($Q\bar{Q}\gamma$ for $Q = t, b$) plays a very important role in the physics of both the Tevatron and the Large Hadron Collider (LHC) to the extent it provides direct information on the third-generation quark electromagnetic couplings and the bottom-quark parton density.

A measurement of $t\bar{t}\gamma$ production can provide a direct test of the $t\bar{t}\gamma$ coupling provided suitable selection cuts can isolate the emission of a hard photon from the produced top-quark pair [1, 2]. Next-to-Leading Order (NLO) QCD corrections to this process have been calculated for on-shell top quarks [3] and for off-shell top quarks [4], where NLO QCD corrections for the decay process have also been taken into account using a narrow-width approximation, and the problem of distinguishing hard-photon emission from production and decay has been addressed.

On the other hand, the associated production of a photon with a $b\bar{b}$ pair is a crucial component of the theoretical prediction for direct-photon production with b jets which, once compared with experiments, will provide a direct access to the bottom-quark parton density in nucleons and help understanding the nature of the b -quark parton distribution function (PDF). Several subtle issues enter the comparison of theoretical predictions with existing and future experimental measurements and progress is still needed to be able to directly constrain the b -quark parton distribution function and investigate the presence of an intrinsic b -quark density in nucleons as opposed to a purely perturbative b -quark density obtained from the evolution of the gluon parton density. Constraining and understanding the b -quark parton density will play a very important role in improving the accuracy with which other crucial processes like the associated production with weak gauge bosons ($W/Z + b$), a background to Higgs production, and the associated production with a scalar/pseudoscalar ($H/A + b$), a clear signal of new physics, can be predicted.

The NLO prediction for direct photon production in association with one b jet has been calculated in the so-called *variable-flavor scheme* (VFS) or *five-flavor-number scheme* (5FNS) [5], where a b -quark parton density is assumed in the initial state and the b quark is treated as massless. On the experimental side, the $\gamma + b + X$ process has been measured at the Tevatron by the D0 collaboration with 1 fb^{-1} [6] and 8.7 fb^{-1} [7] data sets as well as by the CDF collaboration with 86 pb^{-1} [8] and more recently 9.1 fb^{-1} [9] data sets. The

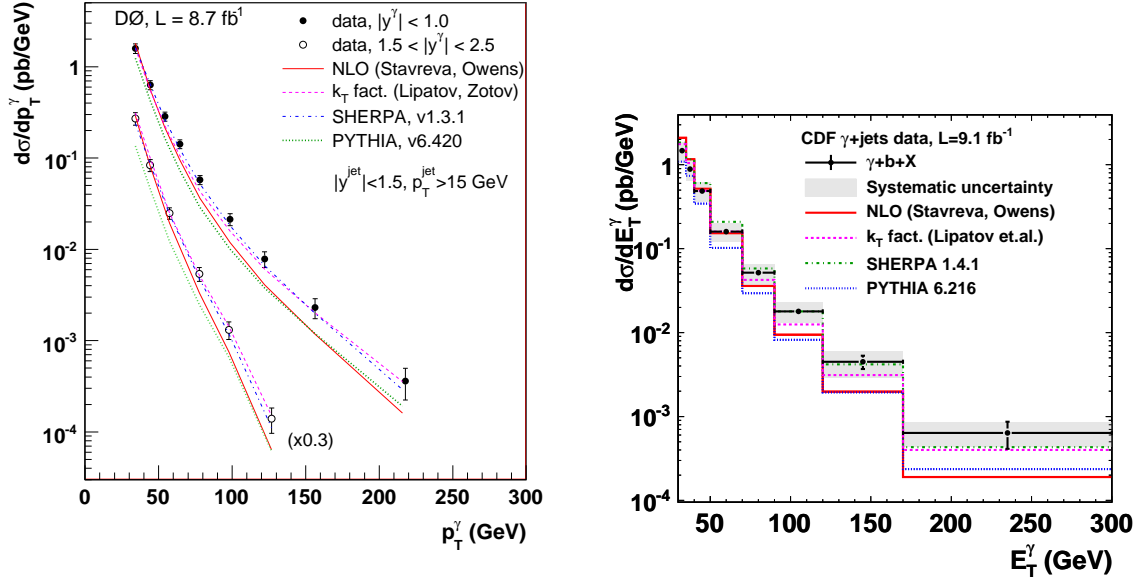


FIG. 1: The photon transverse-momentum distribution measured by the D0 [7] (left) and CDF [9] (right) collaborations for $p\bar{p} \rightarrow \gamma + b + X$ process at the Tevatron in comparison with theoretical predictions.

$p_T(\gamma)$ distributions for the $p\bar{p} \rightarrow \gamma + b + X$ process at the Tevatron from the most recent D0 [7] and CDF [9] results are shown in Fig. 1. The experimental data are compared with the predictions from the VFS/5FNS NLO calculation in [5], as well as other predictions from Pythia [10, 11], Sherpa [12, 13], and a calculation which uses the k_T -factorization approach [14] that contains only partial NLO corrections but selected higher-order effects. In the intermediate to high photon transverse-momentum region, one notices some discrepancies between the data and the VFS/5FNS NLO calculation.

In this paper we present the NLO QCD results for hard-photon production with either one or two b jets, using a *fixed-flavor scheme* (FFS) or *four-flavor-number scheme* (4FNS). The calculation consists of the NLO QCD corrections to $pp(p\bar{p}) \rightarrow b\bar{b}\gamma$, where the b quark is treated as massive and no b -quark parton density is assumed in the initial state¹. Details of the FFS/4FNS calculation are presented in Section II, while various kinematic distributions

¹ We notice that the production of an off-shell photon in association with a $b\bar{b}$ pair at NLO in QCD has been presented in Ref. [15], but cannot be used for on-shell direct photon production

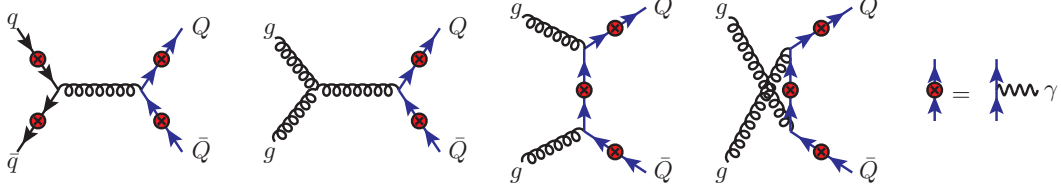


FIG. 2: Tree-level Feynman diagrams for $pp(p\bar{p}) \rightarrow Q\bar{Q}\gamma$ production, corresponding to the $q\bar{q} \rightarrow Q\bar{Q}\gamma$ and $gg \rightarrow Q\bar{Q}\gamma$ subprocesses. For each diagram, the red circled crosses correspond to all possible photon insertions.

for both the $\gamma + b$ and $\gamma + 2b$ jets are presented in Section III, including their theoretical systematic uncertainty. The comparison with CDF and D0 data [7, 9], as well as other existing theoretical results [5], is also discussed in Section III. Finally, Section IV summarizes our conclusions and suggests possible future developments.

II. NLO QCD CORRECTIONS TO $\gamma + 2b$ AND $\gamma + 1b$ JETS

In this section we present the most relevant aspects of the calculation of the $\mathcal{O}(\alpha_s)$ corrections to $pp(p\bar{p}) \rightarrow Q\bar{Q}\gamma$ for $Q = t, b$. The structure of the calculation and the techniques used in its realization are summarized in Sec. II A. A complete discussion of the details can be found in [16]. As briefly mentioned in Sec. I, the case of hard-photon production with one b jet can be addressed using both a 5FNS and a 4FNS approach. We will discuss the comparison between the two approaches in more detail in Sec. II B. Finally, we will introduce and discuss the impact of different choices of photon-isolation prescription in Sec. II C.

A. Structure of $\mathcal{O}(\alpha_s)$ corrections

At tree level the $pp(p\bar{p}) \rightarrow Q\bar{Q}\gamma$ ($Q = t, b$) process consists of two partonic subprocesses, namely $q\bar{q} \rightarrow Q\bar{Q}\gamma$ and $gg \rightarrow Q\bar{Q}\gamma$, as illustrated in Fig. 2. The first order of QCD corrections consist of $\mathcal{O}(\alpha_s)$ virtual one-loop corrections to the tree-level subprocesses as well as $\mathcal{O}(\alpha_s)$ real corrections in the form of three subprocesses with an additional radiated parton, namely $q\bar{q} \rightarrow Q\bar{Q}\gamma + g$, $gg \rightarrow Q\bar{Q}\gamma + g$, and $gq(g\bar{q}) \rightarrow Q\bar{Q}\gamma + q(\bar{q})$.

We have calculated the $\mathcal{O}(\alpha_s)$ virtual one-loop corrections using a Feynman-diagram approach and two independent calculations, based on an in-house code and on the NLOX

package [17] respectively. Both codes relies on the FORM symbolic manipulation program [18] to decompose tensor integrals in terms of tensor-integral coefficients and spinor structures, as well as to interfere the one-loop and tree-level amplitudes. Tensor one-loop integrals are reduced to a linear combination of scalar integrals using various techniques such as the Passarino-Veltman (PV) [19], Denner-Dittmaier [20], and Diakonidis et al. [21] methods. One-loop scalar integrals are evaluated using the QCDLoop package [22].

UV and IR divergences have been extracted using dimensional regularization. UV divergences arising from self-energy and vertex diagrams are cancelled by introducing counterterms for the external fields, the strong coupling, and the heavy-quark mass. The QED coupling does not renormalize at the first order in α_s . IR divergences arising in vertex, box, and pentagon diagrams are cancelled by analogous IR divergences in the real-emission part of the NLO cross section. A detailed discussion of the UV and IR divergences of the $(q\bar{q}, gg) \rightarrow Q\bar{Q}\gamma$ virtual amplitudes is given in Ref. [16].

Real-emission corrections have been computed using a phase-space-slicing method with both a soft (δ_s) and a collinear (δ_c) cutoffs to isolate and compute the IR singular terms of the cross section and the corresponding finite contributions. The cancellation of IR singularities between virtual and real corrections has been verified and the independence of the physical cross section of the choice of δ_s and δ_c has been thoroughly proved [16].

On top of internal independent cross checks, we have also interfaced our routines for the one-loop virtual corrections with the Sherpa [12, 13] Monte Carlo event generator, which implements the Catani-Seymour dipole-subtraction formalism [23, 24], and found agreement at the level of the partonic NLO cross sections.

B. 4FNS vs 5FNS

The NLO QCD calculation of $Q\bar{Q}\gamma$ hadronic production allows us to study the phenomenology of both $t\bar{t}\gamma$ and $b\bar{b}\gamma$ production at the Tevatron and the LHC. Practically, one can simply specify the mass ($m_Q = m_t$ or m_b) as well as the charge of the heavy quark ($Q_Q = Q_t$ or Q_b) to switch from one to the other. The case of a final-state bottom-quark pair, however, requires some extra care due to both theoretical and experimental issues.

$t\bar{t}\gamma$ is calculated assuming five massless quark flavors, i.e. in a 5FNS. The short lifetime of the top quark allows it to decay (dominantly via $t \rightarrow bW$) before it hadronizes. In

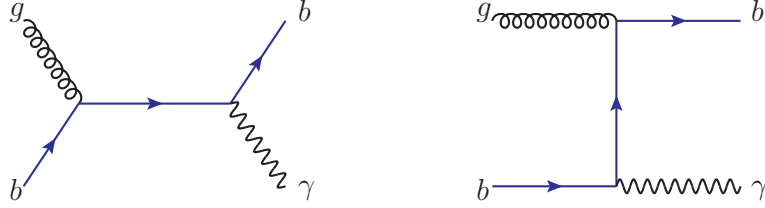


FIG. 3: Tree-level Feynman diagrams for $pp(p\bar{p}) \rightarrow b(\bar{b})\gamma + X$ production in the 5FNS, corresponding to the $gb \rightarrow b\gamma$ subprocess.

calculating inclusive observables in $t\bar{t}\gamma$ production, the top quark can be considered as a stable final state, as done in [3] and [4]. Alternatively, one can consider more exclusive modes, where the decay of the top-quark pair is also explicitly accounted for. The study of $t\bar{t}\gamma$ production including NLO QCD corrections both in the production and decay stages is done in [4]. We have reproduced results for a stable $t\bar{t}$ pair and found full agreement with Ref. [4], for the same setup of external parameters². Since a comparison with Ref. [3] had already been presented in Ref. [4], we have not investigated it any further in this context.

On the other hand, a bottom quark in the final state will form a jet that can be detected experimentally via b -tagging, i.e. imposing specific cuts on some b -jet kinematic variables, typically its transverse momentum and pseudorapidity. In this paper we consider the following cases:

- at least two b jets observed in the final state ($pp(p\bar{p}) \rightarrow b\bar{b}\gamma + X$, “2 b -tag”),
- at least one b jet observed in the final state ($pp(p\bar{p}) \rightarrow b(\bar{b})\gamma + X$, “1 b -tag”),

The NLO QCD calculation of the 2 b -tag case can only proceed in the 4FNS, where one assumes only four massless quark flavors, the b quark is treated as massive, and does not appear in the initial state. This is exactly the $Q\bar{Q}\gamma$ calculation presented in this paper with $Q = b$ ($m_Q = m_b$, $Q_Q = Q_b$). On the other hand, the NLO QCD calculation of the 1 b -tag case can be done using both the 4FNS and the 5FNS, where instead the b flavor is treated as massless and an initial state b -quark density is introduced. The tree level processes are different and are given in Fig. 2 for the 4FNS and in Fig. 3 for the 5FNS. The

² Full details can be found in [16]

TABLE I: List of subprocesses that contribute to the LO and NLO VFS/5FNS calculation of $pp(p\bar{p}) \rightarrow \gamma b + X$ process, with $i = q, \bar{q}$ and $Q = b, \bar{b}$.

Part	Subprocess
LO and NLO virtual	$Qg \rightarrow \gamma Q$
NLO real	$Qg \rightarrow \gamma Qg$
NLO real	$iQ \rightarrow \gamma Qi$
NLO real	$QQ \rightarrow \gamma QQ$
NLO real	$q\bar{q} \rightarrow \gamma b\bar{b}$
NLO real	$gg \rightarrow \gamma b\bar{b}$

$\mathcal{O}(\alpha_s)$ corrections are then calculated as one-loop virtual and real-emission corrections to the corresponding tree level processes. The 4FNS case is already discussed in Sec. II A. For the 5FNS case we list the processes entering the NLO QCD calculation and their role in Table II B. In both cases one requires that at least one b jet is reconstructed and tagged in the final state. In the 4FNS, the selected sample will of course also include events with two b jets, as well as events with one or two b jets and a light jet.

As it is well known, the 5FNS approach naturally arise from the 4FNS calculation when one considers that the integration over the phase space of the final-state untagged b quark generates logarithms of the form $\ln(Q/m_b)$, where technically Q is the upper bound on the p_T of the unobserved b -quark. For large Q ($Q \gg m_b$) these logarithms can become large and spoil the convergence of the perturbative expansion of the cross section. These logarithms however can be factored out and resummed using renormalization-group arguments in the form of DGLAP equations by introducing a bottom-quark PDF,

$$f_b^{p/\bar{p}}(x, \mu) = \frac{\alpha_s(\mu)}{\pi} \ln\left(\frac{Q}{m_b}\right) \int_x^1 \frac{dy}{y} P_{gq}\left(\frac{x}{y}\right) f_g^{p/\bar{p}}(x, \mu), \quad (1)$$

where $f_g^{p/\bar{p}}(x, \mu)$ is the gluon PDF and P_{gq} is the Altarelli-Parisi splitting function for $g \rightarrow q\bar{q}$. By defining the b -quark PDF, the 5FNS approach restructures the calculation as an

expansion in terms of α_s and the potentially large $\ln(Q/m_b)$ logarithms. As a result of the 5FNS approach, the process where at least one b jet is identified in the final state now starts at LO with the $gb \rightarrow b\gamma$ subprocesses shown in Fig. 3, with $m_b = 0$. If the 5FNS approach emphasizes the role of these *initial-state* logarithms, and add stability to the theoretical results by resumming leading and subleading families of such logarithms, it nevertheless neglects other contributions that do not appear in the 5FNS calculation (as one can notice by comparing the list of subprocesses and their $\mathcal{O}(\alpha_s)$ corrections) because they are not directly affected by the resummation logarithms. At the same time, different subprocesses enter at different perturbative orders in the 4FNS or 5FNS calculation of the same hadronic process. For instance, in the case of $pp(p\bar{p}) \rightarrow \gamma + b + X$, the $q\bar{q} \rightarrow b\bar{b}\gamma$ subprocess enters at lowest order in the 4FNS calculation, while it counts as an $\mathcal{O}(\alpha_s)$ correction in the 5FNS calculation. As such, it enters the 5FNS calculation as a tree-level process, while it is included in the 4FNS calculation together with its own $\mathcal{O}(\alpha_s)$ corrections. If a particular subprocess, as it is the case for $q\bar{q} \rightarrow b\bar{b}\gamma$, dominates in a given kinematic regime or at a given center-of-mass energy, including it at tree-level or at the one-loop level can make a drastic difference both quantitatively (one-loop corrections may be large) and qualitatively (NLO corrections in general reduce the theoretical systematic uncertainty from renormalization- and factorization-scale dependence). Therefore, even if 4FNS and 5FNS approaches are just two different ways of reorganizing the QCD perturbative expansion of a given physical observable, they may show significantly different behaviors within the first few orders of the perturbative expansion. Moreover, being the logarithms resummed in the 5FNS approach of fundamental kinematic nature, the interpretation of the comparison between the 4FNS and 5FNS approaches may require to look at both total and differential cross sections. In Sec. IIID we will quantitatively illustrate the comparison between the two different approaches and in Sec. IIIE we will discuss the comparison of both predictions with both CDF and D0 data.

C. Photon isolation

Photons in a hadronic environment are usually distinguished into *prompt photons*, when they are directly produced in the hard interaction, and *secondary photons*, when they originate from the hadronization phase of a hadronic jet or the decay of unstable hadrons (e.g.

$\pi^0 \rightarrow \gamma\gamma$). While the production of prompt photons can be described in perturbation theory, the production of secondary photons can only be modeled and can therefore introduce a large parametric uncertainty in any given calculation. Since secondary photons tend to preeminently occur in regions of the detector with abundant hadronic activity, in particular within or close to jets, their effect can be eliminated by imposing so-called *isolation cuts* which specifically limit the hadronic activity around a given photon. Prompt photons become then *isolated photons* and can be easily disentangled.

The main theoretical caveat in implementing a given prescription to *isolate* prompt photons from the hard interaction is that such procedure can veto regions of phase space responsible for soft QCD radiation and could therefore spoil the cancellation of infrared divergences between virtual and real corrections in a perturbative QCD calculation. As soon as some residual hadronic activity is admitted in the region around the photon, very energetic collinear final-state partons can produce a small parton-photon invariant mass and the corresponding collinear divergences need therefore to be reabsorbed into suitable fragmentation functions³. To extract the quark-photon final state collinear singularity encountered in our calculation, we have also used the phase-space slicing method. The cross section for prompt-photon production is then given by,

$$\sigma^\gamma(\mu_R, \mu_F, M_F) = \sigma_{\text{direct}}^\gamma(\mu_R, \mu_F) + \int_0^1 dz \sum_i \sigma_i(\mu_R, \mu_F, M_F) D_{i \rightarrow \gamma}(z, M_F), \quad (2)$$

where $\sigma_{\text{direct}}^\gamma$ represents the cross section for the direct component while σ_i denotes the cross section for the production of a parton i that further fragments into a photon. The probability for a parton i to fragment into a photon is represented by the corresponding photon fragmentation functions (FFs), $D_{i \rightarrow \gamma}(z, M_F)$, where z is the fraction of the parton momentum that is carried by the photon, and M_F is the fragmentation scale. Examples of available FFs in the literature are by Bourhis, Fontannaz and Guillet (set I and II) [25] and by Gehrmann-de Ridder and Glover [26]. Fragmentation functions for final-state partons, like parton distribution functions for initial-state partons, are intrinsically non perturbative and introduce into the calculation the same kind of uncertainty in the modeling

³ In our calculation this happens in the $qg \rightarrow Q\bar{Q}\gamma + q$ channel when the photon becomes collinear to the massless final state quark. Notice that the hard-photon cut that is imposed on the transverse momentum of the photon (see Sec. III A) eliminates initial-state parton-photon singularities and all soft-photon singularities.

of secondary photons that one originally wanted to eliminate. How relevant the contribution of fragmentation functions is depends on the chosen isolation prescription.

In our calculation we used two main prescriptions that we denote as *fixed-cone* and *smooth-cone* prescriptions. The *fixed-cone* prescription is commonly used in experiments and limits the hadronic activity inside a cone of radius R_0 around the photon by imposing that the hadronic transverse energy inside the cone does not exceed a maximum value, E_T^{\max} , set by the experiment, i.e.

$$\sum_{\in R_0} E_T(\text{had}) < E_T^{\max} , \quad (3)$$

where $R_0 = \sqrt{\Delta\eta^2 + \Delta\phi^2}$, and $\Delta\eta$ and $\Delta\phi$ are the pseudorapidity and azimuthal angle differences between the photon and a jet. After the isolation cut, the value of z is typically large, and since the FFs are dominant in the low z region, the isolation procedure suppresses the fragmentation contribution substantially.

Alternatively, the *smooth-cone* isolation prescription introduced in Ref. [27] limits the hadronic activity around a photon by imposing a threshold on the transverse hadronic energy within a cone about the photon that varies with the radial distance from the photon, i.e

$$\sum_i E_T^i \theta(R - R_{i,\gamma}) < \epsilon E_T^\gamma \left(\frac{1 - \cos R}{1 - \cos R_0} \right) \quad \text{for all } R \leq R_0, \quad (4)$$

where the i summation runs over all final-state partons in the process and $E_T^{i(\gamma)}$ is the transverse energy of the parton (photon). R_0 is the size of the isolation cone, ϵ is an isolation parameter of $O(1)$, and

$$R_{i,\gamma} = \sqrt{(\Delta\eta_{i,\gamma})^2 + (\Delta\phi_{i,\gamma})^2}.$$

The θ -function ensures that the i summation only receives contributions from partons that lie inside the isolation cone. $R = R_{i,\gamma}$ if there is only one parton inside the isolation cone, while for the case where more than one parton is present inside the cone, R is the largest $R_{i,\gamma}$ inside the cone. The r.h.s of Eq. 4 vanishes as $R \rightarrow 0$, thus the collinear configurations are suppressed while soft radiation is allowed to be present arbitrarily close to the photon. Since the collinear configurations are completely removed, there is no fragmentation component in Eq. 2.

The fragmentation contribution in the $pp(p\bar{p}) \rightarrow b\bar{b}\gamma$ calculation is included at $\mathcal{O}(\alpha_s^2)$. Due to the photon isolation requirement, a photon cannot fragment from the tagged b/\bar{b}

quark. In the $2b$ -tag case (as well as in $t\bar{t}\gamma$ production), the photon can only fragment off a light parton j , i.e. σ_i in Eq. 2 is the cross section for the $pp(p\bar{p}) \rightarrow b\bar{b}j$ process calculated at LO, ($\sigma_i = \sigma_{LO}(pp(p\bar{p}) \rightarrow b\bar{b}j)$). We notice that $\sigma_{LO}(pp(p\bar{p}) \rightarrow b\bar{b}j)$ is finite since we impose a cut on the photon transverse momentum. For the $1b$ -tag case, in addition to the same contribution present in the $2b$ -tag case, the photon can also fragment off an unidentified b/\bar{b} quark. The LO $pp(p\bar{p}) \rightarrow b\bar{b}j$ cross section is divergent in this case since the light parton in the final state can be soft and/or collinear. To overcome this problem, we should start from the $pp(p\bar{p}) \rightarrow b\bar{b}$ cross section at NLO in QCD. We have implemented the $\mathcal{O}(\alpha_s)$ real corrections to $pp(p\bar{p}) \rightarrow b\bar{b}$ using a phase-space slicing method with two cutoffs, while we have taken the $\mathcal{O}(\alpha_s)$ virtual corrections from the MCFM package [28]. We also notice that when the photon is fragmented off of a b/\bar{b} quark, terms proportional to $\ln(M_F^2/m_b^2)$, arising from the collinear configuration of the $b \rightarrow b\gamma$ splitting in the (direct) $pp(p\bar{p}) \rightarrow b\bar{b}\gamma$ process, have to be subtracted to avoid double counting since those terms have been included and resummed in the b quark-to-photon fragmentation function via DGLAP evolution equations.

III. RESULTS

In this Section we present numerical results for the inclusive hard-photon production in association with a bottom- and antibottom-quark pair at hadron colliders, $pp(p\bar{p}) \rightarrow b\bar{b}\gamma + X$ including the full effect of NLO QCD corrections as described in Section II. We distinguish the case where at least two b jets are identified in the final state ($\gamma + 2b + X$, or $2b$ -tag), and the case where at least one b jet is identified in the final state ($\gamma + b + X$, or $1b$ -tag). For the $1b$ -tag case, we compare the results obtained from our FFS/4FNS calculation with the results obtained from the VFS/5FNS calculation at NLO in QCD. Finally, we provide a first comparison of the FFS/4FNS results for $\gamma + b + X$ with the measurements by the CDF and D0 collaborations.

A. The Setup

The numerical results for $b\bar{b}\gamma$ production are presented for proton-proton collisions at the LHC with $\sqrt{s} = 8$ TeV and proton-antiproton collisions at the Tevatron with $\sqrt{s} = 1.96$ TeV. The following SM parameters are used in the numerical evaluation,

Parameter	Value
m_b	4.62 GeV
m_t	173.2 GeV
α	1/137

where m_t , m_b , and α are the top-quark mass, bottom-quark mass and electromagnetic coupling constant respectively. The bottom quark is treated as massive, with the number of light quarks entering the fermion loop set to $n_f = 4$. This means that any fermion loop that enters in the virtual corrections consists of four light-quark, one bottom-quark, and one top-quark loop. The LO results use the CTEQ6L1 PDF set [29] and the one-loop evolution of the strong coupling, α_s , with $\alpha_s^{\text{LO}}(M_Z) = 0.13$, while the NLO results use the CT10nlo_nf4 PDF set [30] and the two-loop evolution of α_s , with $\alpha_s^{\text{NLO}}(M_Z, n_f = 4) = 0.1127$. The renormalization and factorization scales are set equal to one another, and the central scale is chosen to be a dynamical scale given by the transverse momentum of the photon, i.e.

$$\mu_R = \mu_F = \mu_0 = p_T(\gamma), \quad (5)$$

for both the $2b$ - and $1b$ -tag case. We have explored other possibilities and will comment on our choice in Sec. IIIB. The residual scale dependence of the LO and NLO cross sections is studied by varying $\mu = \mu_R = \mu_F$ by a factor of four around the central value given in Eq. (5). Independent variation of μ_R and μ_F could be considered but the choice of a dynamical scale makes it unpractical. We have instead allowed for a pretty conservative variation by a factor of four around the central value μ_0 (instead of the traditional factor of two).

The selection cuts for the photon are: $p_T(\gamma) > 30$ GeV and $|\eta(\gamma)| < 1$ for the Tevatron [7, 9], and $p_T(\gamma) > 25$ GeV and $|\eta(\gamma)| < 1.37$ for the LHC [31]. We notice that the photon's rapidity ($y(\gamma)$) and pseudorapidity ($\eta(\gamma)$) coincide. We also notice that the Tevatron D0 experiment also considered a forward rapidity region, $1.5 < |\eta(\gamma)| < 2.5$. We will not introduce it as a default in presenting most of the results of our study but we will consider it in Sec. IIIE to compare with D0 results. Both bottom-quark and the light-quark jets are clustered using the anti- k_T jet algorithm, with pseudo-cone size $R = 0.4$, and are required to pass the following selection cuts:

$$\begin{aligned} \text{Tevatron: } & p_T(b, j) > 20 \text{ GeV, } |\eta(b, j)| < 1.5, \quad [7, 9] \\ \text{LHC: } & p_T(b, j) > 25 \text{ GeV, } |\eta(b, j)| < 2.1, \quad [32] \end{aligned}$$

where $\eta(b, j)$ denotes the pseudorapidity of the corresponding jet. Since massless jets (j) in our calculation are always single-parton objects, their pseudorapidity and rapidity also coincide. Finally, since we consider inclusive observables, we include events with both 0 and 1 identified light-parton jet in our calculation.

As explained in Sec. II C, we use both a fixed-cone and a smooth-cone isolation criteria [27] to reduce the hadronic activity around the hard photon and minimize the contribution from photon fragmentation. We will compare the two approaches when relevant and show the remaining results using as default one of the two options as specified. We notice that, in contrast to the top-quark case ($t\bar{t}\gamma$), here the bottom quarks have to be included in the hadronic energy contribution, following the prescription described in Sec. II C.

B. $pp(p\bar{p}) \rightarrow b\bar{b}\gamma + X$: at least two b jets identified in the final state

In this section we present results for $b\bar{b}\gamma$ production where at least two b jets are tagged in the final state. At NLO in QCD this includes configurations in which the jets consist of just a single b (or \bar{b}) quark as well as configurations in which the b or \bar{b} jet include also a light parton. To identify a hard photon we have used both a smooth-cone and a fixed-cone isolation criterion and noticed minimal differences in the results. Therefore in this section we limit ourselves to results that have been obtained using the fixed-cone isolation criterion in Eq. 3, with the following parameters:

$$\begin{aligned} \text{Tevatron: } R_0 &= 0.4, E_T^{\text{max}} = 2 \text{ GeV, [9]} \\ \text{LHC: } R_0 &= 0.4, E_T^{\text{max}} = 5 \text{ GeV, [32].} \end{aligned}$$

We also use Set II of Bourhis, Fontannaz and Guillet [25] for the photon fragmentation functions.

The impact of NLO QCD corrections on the perturbative stability of the total cross section is well illustrated in Fig. 4 where we show the dependence of the total cross section on the renormalization/factorization scale at the Tevatron and at the LHC. The impact of QCD corrections depends on the chosen scale and is always large. For renormalization/factorization scales that vary in the $\mu_0/4 \leq \mu \leq 4\mu_0$ interval, we find K -factors (defined as $K = \sigma_{NLO}/\sigma_{LO}$ with σ_{NLO} and σ_{LO} calculated with the setup defined in this Section) that range from 1 to 1.8 at the Tevatron, and from 1.5 to 1.8 at the LHC.

TABLE II: Total cross section for $pp(p\bar{p}) \rightarrow b\bar{b}\gamma + X$ production with at least two b jets tagged in the final state at the Tevatron ($\sqrt{s} = 1.96$ TeV) and the LHC ($\sqrt{s} = 8$ TeV), at LO and NLO, together with their K -factor. The uncertainties are due to the dependence on the renormalization/factorization scale obtained by evaluating the cross section at $\mu_R = \mu_F = p_T(\gamma)/4$ for the upper value and at $\mu_R = \mu_F = 4p_T(\gamma)$ for the lower value. The integration errors are well below 1% .

Collider	σ_{LO} [pb]	σ_{NLO} [pb]	K -factor
Tevatron at $\sqrt{s} = 1.96$ TeV	$2.18^{+43\%}_{-104\%}$	$3.06^{+30\%}_{-40\%}$	$1 - 1.8$
LHC at $\sqrt{s} = 8$ TeV	$29.4^{+38\%}_{-73\%}$	$46.6^{+30\%}_{-60\%}$	$1.5 - 1.8$

What is however more interesting is that the residual scale dependence turns out to be quite substantial at both the Tevatron and LHC even when NLO QCD corrections are included, with only a very little improvement observed at the Tevatron. To study the origin of the strong scale dependence, we look at the scale dependence of the different subprocesses that contribute to the total NLO cross section, as shown in Fig 4. At the Tevatron the $q\bar{q}$ subprocess dominates over the gg subprocess, while the opposite happens at the LHC, both at LO and at NLO. The $qg + \bar{q}g$ subprocess (from now on denoted simply as qg) enters only at NLO and, although never dominant, plays an important role at the LHC. It is interesting to notice that both at the Tevatron and at the LHC, the scale dependence of the $q\bar{q}$ and gg subprocesses are improved at NLO, as we can see from the plateau in the scale-dependence plot, while the residual scale dependence is due to the qg subprocess that comes in at NLO as a tree level contribution and introduces therefore a large scale dependence.

The choice of a dynamical scale is quite natural for this process, since there is no preferred fixed hard scale to be chosen (like $\mu = m_t$ for $t\bar{t}\gamma$ production). To investigate the adequacy of choosing the photon transverse momentum, $p_T(\gamma)$, as dynamical scale, we have tried four different central-scale choices to study the stability of each subprocess with respect to different dynamical scales. From the four plots that are shown in Fig. 5, where we take the

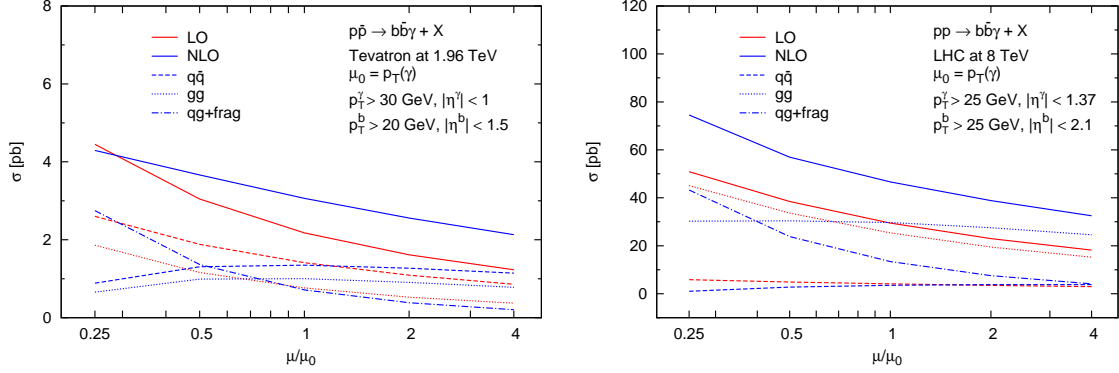


FIG. 4: Dependence of the LO (red) and NLO (blue) cross section for $pp \rightarrow b\bar{b}\gamma + X$ (at least two b jets identified in the final state) on the renormalization/factorization scale at the Tevatron with $\sqrt{s} = 1.96$ TeV (left) and at the LHC with $\sqrt{s} = 8$ TeV (right). Both the total cross section (solid) and the contributions of the individual subprocesses, $q\bar{q}$ (dashed), gg (dotted), and qg (dash-dotted) are shown.

LHC at $\sqrt{s} = 8$ TeV case as an example, it is evident that the NLO cross sections are overall shifted when a different central scale is chosen. By investigating the contribution from each subprocess, we see that the shifting of the total NLO cross section is driven by the qg subprocess and is therefore part of the theoretical uncertainty introduced by the opening of this new channel at NLO. On the other hand, both the $q\bar{q}$ and gg subprocesses are relatively insensitive to the different choice of dynamical scale. In presenting our results for $b\bar{b}\gamma$ production we have therefore chosen the scale to be fixed by $p_T(\gamma)$ and have conservatively allowed it to vary by a factor of four about the central value $\mu_0 = p_T(\gamma)$, as explained earlier. Results are summarized in Table. II, where we present both LO and NLO cross sections for the Tevatron at $\sqrt{s} = 1.96$ TeV and the LHC at $\sqrt{s} = 8$ TeV. The uncertainty due to scale variation is obtained by evaluating the cross section at $\mu_R = \mu_F = p_T(\gamma)/4$ ($\mu_R = \mu_F = 4p_T(\gamma)$) for the upper (lower) value.

We now turn to the phenomenologically more interesting case of differential distributions. In Figs. 6 and 7 and Figs. 8 and 9 we show the photon and the leading b -jet (b_1) transverse-momentum distributions as well as the photon pseudorapidity and photon to leading b -jet separation ($R(\gamma, b_1)$) distributions at the Tevatron and the LHC respectively. The bands in each figure represent the variation of the differential cross section (bin-by-bin) when the

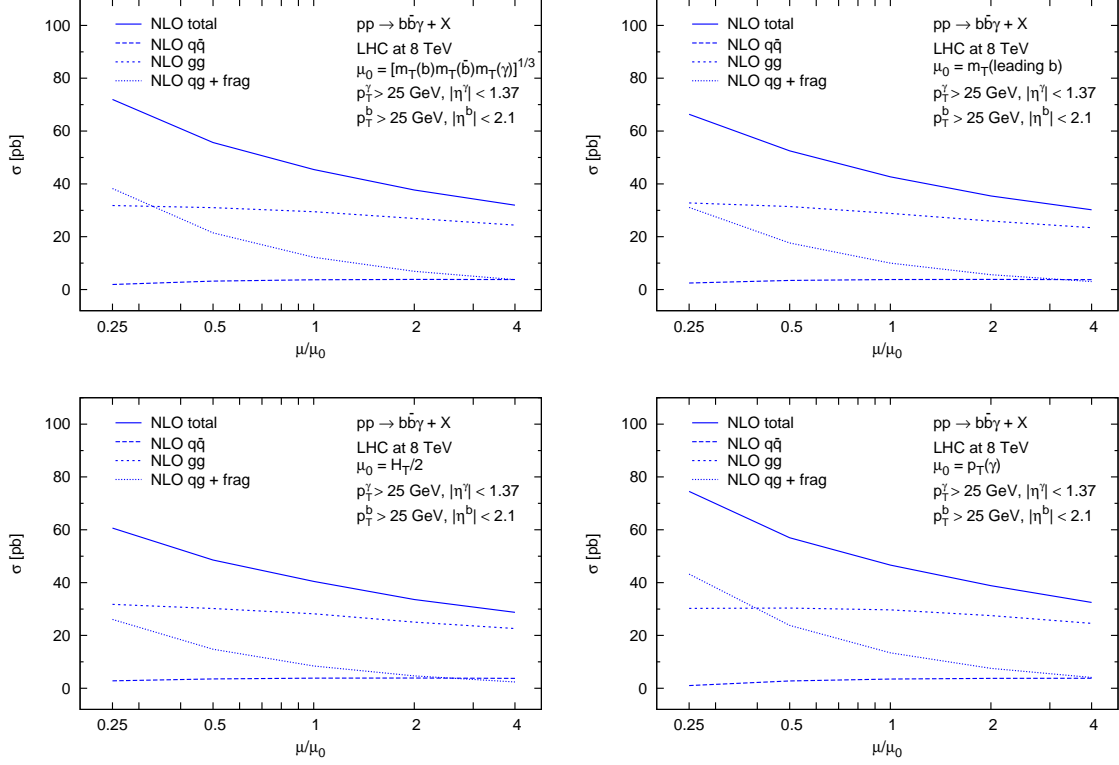


FIG. 5: Scale dependence of the NLO total cross section (solid) for $pp \rightarrow b\bar{b}\gamma + X$ (at least two b jets identified in the final state) and of the individual $q\bar{q}$ - (dashed), gg - (dotted), and qg - (dash-dotted) subprocess contributions for four different choices of the central scale: $\mu_0 = (m_T(b)m_T(\bar{b})m_T(\gamma))^{1/3}$ (top-left), $\mu_0 = m_T(\text{leading } b)$ (top-right), $\mu_0 = H_T/2 = \sum_{i=b,\bar{b},\gamma} E_T^i/2$ (bottom-left), $\mu_0 = p_T(\gamma)$ (bottom-right), at the LHC with $\sqrt{s} = 8$ TeV.

renormalization and factorization scales ($\mu_R = \mu_F$) are varied in the range $\mu_0/4 \leq \mu \leq 4\mu_0$, with $\mu_0 = p_T(\gamma)$. The lower window of each figure gives the bin-by-bin K -factor. The impact of the NLO QCD corrections on the differential distributions is sizable in both cases. At the Tevatron, the K -factor for both the $p_T(\gamma)$ and $p_T(b_1)$ distributions decreases as p_T grows, while the opposite is true at the LHC. For the photon pseudorapidity distribution, the K -factor is quite large at the LHC and the shape of the distribution at both the Tevatron and the LHC slightly changes at NLO, becoming flatter due to less photon events that populate the perpendicular direction with respect to the beam axis. In the $R(\gamma, b_1)$ distribution we observe an accidental pinching of the scale variation band at $R(\gamma, b_1) \sim 2.4 - 2.6$. The K -factor is also not well-defined for $R(\gamma, b_1) < 1.5 - 1.7$, where at LO there is no event.

TABLE III: Total cross section for $pp(p\bar{p}) \rightarrow b(\bar{b})\gamma + X$ production with at least one b jet tagged in the final state at the Tevatron ($\sqrt{s} = 1.96$ TeV) and the LHC ($\sqrt{s} = 8$ TeV), at LO and NLO, together with their K -factors. The uncertainties are due to the dependence on the renormalization/factorization scale obtained by evaluating the cross section at $\mu = p_T(\gamma)/4$ for the upper value and at $\mu = 4p_T(\gamma)$ for the lower value. The integration errors are well below 1%.

Collider	σ_{LO} [pb]	σ_{NLO} [pb]	K -factor
Tevatron at $\sqrt{s} = 1.96$ TeV	$14.3^{+44\%}_{-108\%}$	$23.9^{+36\%}_{-63\%}$	1.3 – 1.9
LHC at $\sqrt{s} = 8$ TeV	$299^{+35\%}_{-59\%}$	$405^{+32\%}_{-60\%}$	1.3 – 1.4

The strong residual scale dependence at NLO is also manifest in the differential distributions, in particular at the LHC where in Fig. 8, both for $p_T(\gamma)$ and $p_T(b_1)$, the NLO bands are as large as the LO bands, in the whole p_T region. In contrast, at the Tevatron, the NLO bands are as large as the LO bands at low p_T and as the p_T increases the NLO bands are noticeably shrinking. This can be understood by looking at the contribution of the different subprocesses to the NLO differential distribution as shown in Figs. 10 and 11. At the LHC, both for $p_T(\gamma)$ and $p_T(b_1)$, although the gg subprocess dominates, the contribution of the qg subprocess, which suffers from strong scale dependence, is quite large. On the other hand, at the Tevatron, although in the low- p_T region the gg and qg subprocesses dominate, starting from the intermediate- p_T region, the $q\bar{q}$ subprocess, which receives quite considerable improvement in the scale dependence when the NLO QCD corrections are included, starts to dominate while the contributions of the gg and qg subprocesses drop rapidly.

C. $pp(p\bar{p}) \rightarrow b(\bar{b})\gamma + X$: at least one b jet identified in the final state

In this section we present the numerical results for $b\bar{b}\gamma$ production where at least one b jet is tagged in the final state. This set of events include events with 2 b jets (see Sec. III B) as well as events with 1 b jet that can result from either a single b or \bar{b} as well as from the

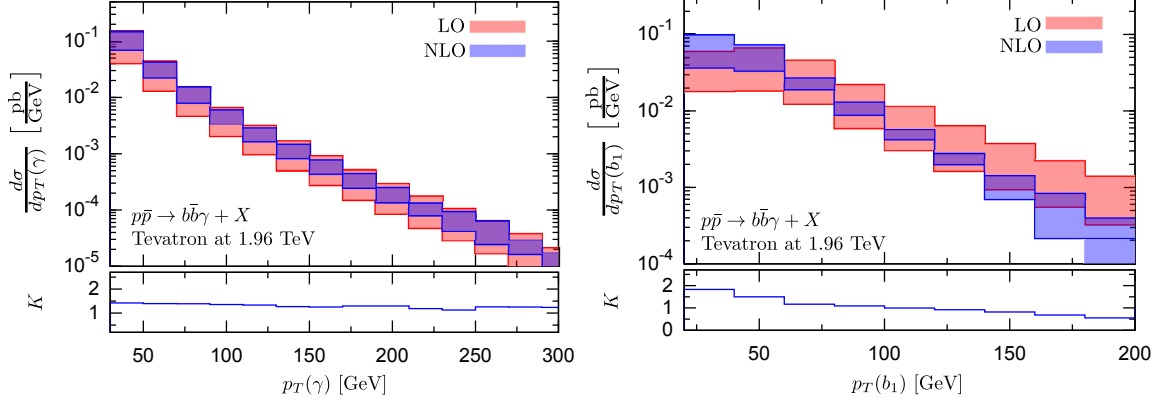


FIG. 6: The upper plots show the transverse-momentum distributions of the photon (left) and the leading b jet (right) for $p\bar{p} \rightarrow b\bar{b}\gamma + X$ (at least two b jets identified in the final state) at the Tevatron with $\sqrt{s} = 1.96$ TeV. The bands correspond to the variation of the renormalization and factorization scales in the interval $\mu_0/4 < \mu < 4\mu_0$. The lower plots show the bin-by-bin K -factor for the corresponding distributions.

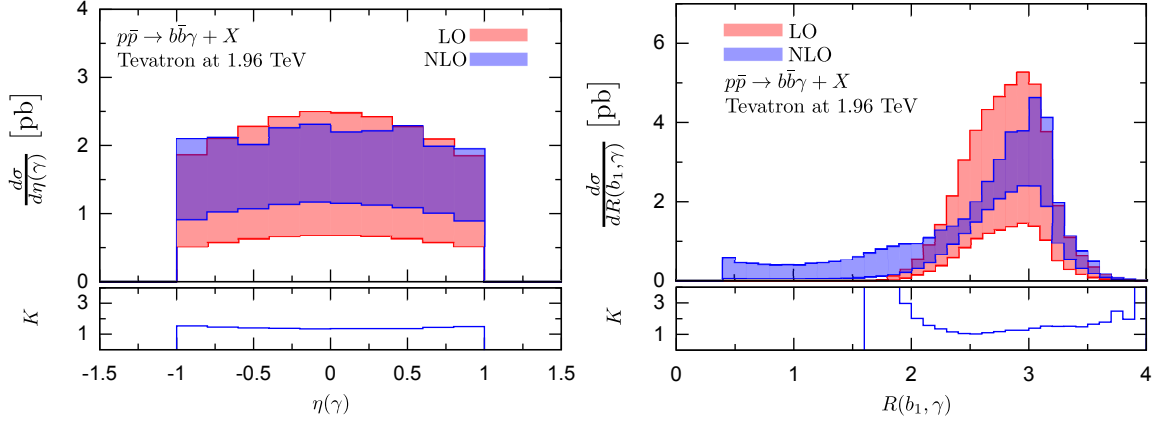


FIG. 7: The upper plots show the pseudorapidity distribution of final-state photon (left) and the separation between the leading b jet and the photon (right) for $p\bar{p} \rightarrow b\bar{b}\gamma + X$ (at least two b jets identified in the final state) at the Tevatron with $\sqrt{s} = 1.96$ TeV. The bands correspond to the variation of the renormalization and factorization scales in the interval $\mu_0/4 < \mu < 4\mu_0$. The lower plots show the bin-by-bin K -factor for the corresponding distributions.

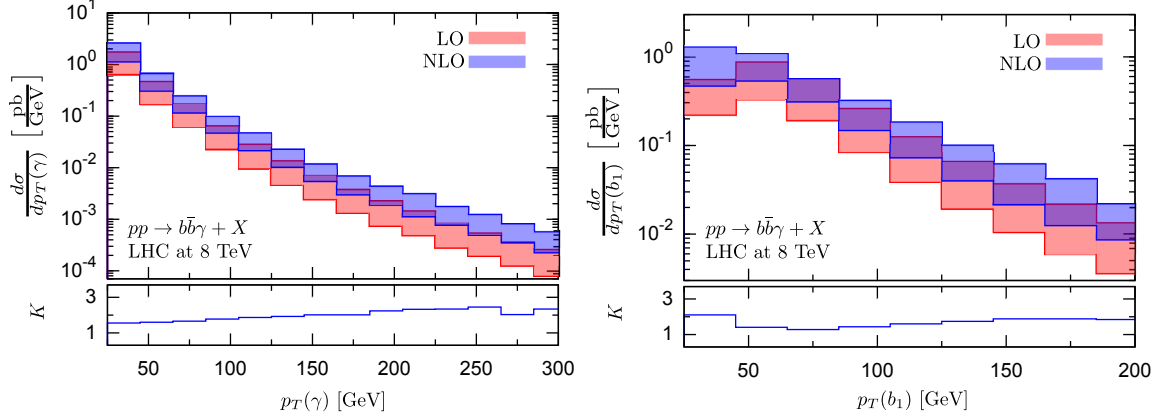


FIG. 8: The upper plots show the transverse-momentum distributions of the photon (left) and the leading b jet (right) for $pp \rightarrow b\bar{b}\gamma + X$ (at least 2 b jets identified in the final state) at the LHC with $\sqrt{s} = 8$ TeV. The bands correspond to the variation of the renormalization and factorization scales in the interval $\mu_0/4 < \mu < 4\mu_0$. The lower plots show the bin-by-bin K -factor for the corresponding distributions.

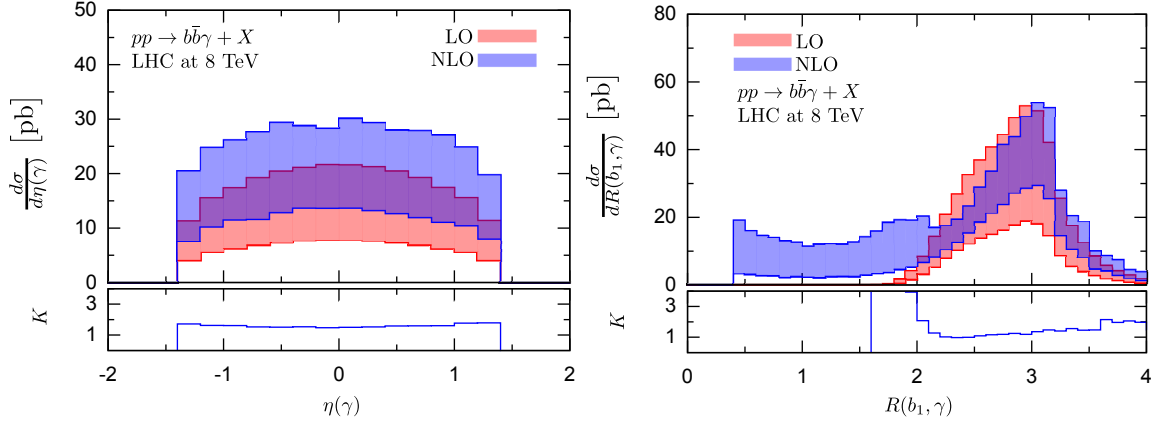


FIG. 9: The upper plots show the pseudorapidity distribution of the photon (left) and the separation between the leading b jet and the photon (right) for $pp \rightarrow b\bar{b}\gamma + X$ (at least two b jets identified in the final state) at the LHC with $\sqrt{s} = 8$ TeV. The bands correspond to the variation of the renormalization and factorization scales in the interval $\mu_0/4 < \mu < 4\mu_0$. The lower plots show the bin-by-bin K -factor for the corresponding distributions.

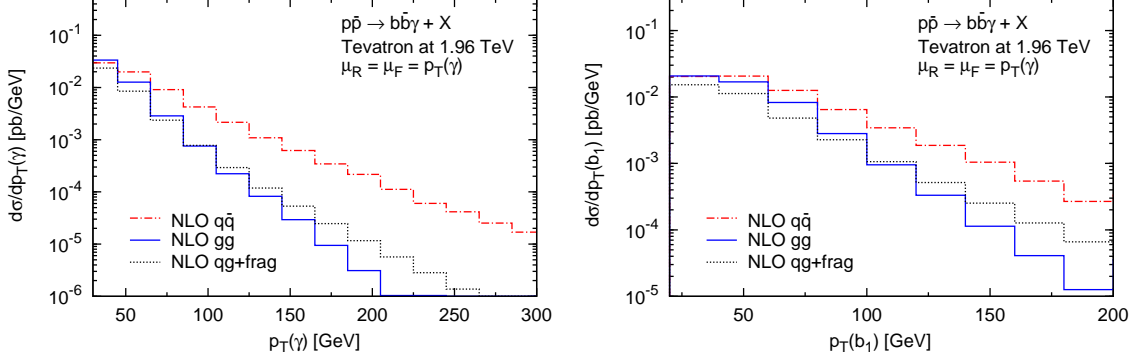


FIG. 10: Individual contributions of the $q\bar{q}$ (red), gg (blue), and qg (black) subprocesses to the transverse-momentum distributions of the photon (left) and the leading b jet (right) for $p\bar{p} \rightarrow b\bar{b}\gamma + X$ (at least two b jets identified in the final state) at the Tevatron with $\sqrt{s} = 1.96$ TeV, and $\mu_R = \mu_F = p_T(\gamma)$.

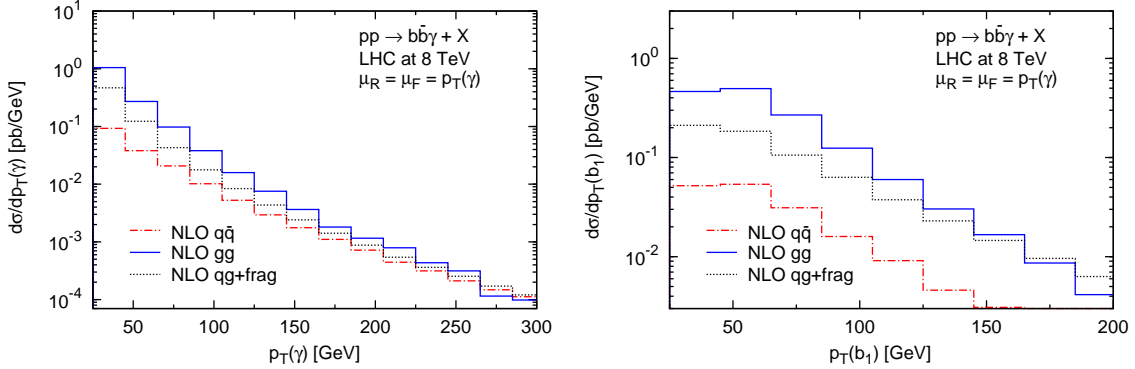


FIG. 11: Individual contributions of the $q\bar{q}$ (red), gg (blue), and qg (black) subprocesses to the transverse-momentum distributions of the photon (left) and the leading b jet (right) for $pp \rightarrow b\bar{b}\gamma + X$ (at least two b jets identified in the final state) at the LHC with $\sqrt{s} = 8$ TeV, and $\mu_R = \mu_F = p_T(\gamma)$.

recombination of b or \bar{b} with a light parton (quark or gluon), of b and \bar{b} themselves, or of b , \bar{b} , and a light parton into a b jet that passes the selection cuts. As before, we have used both a smooth-cone and a fixed-cone isolation criteria to identify a hard photon. We notice a slightly bigger dependence on this choice with respect to the $2b$ -tagging case, but still very small. Therefore we present most results using the fixed-cone isolation criterion (see Eq. 3),

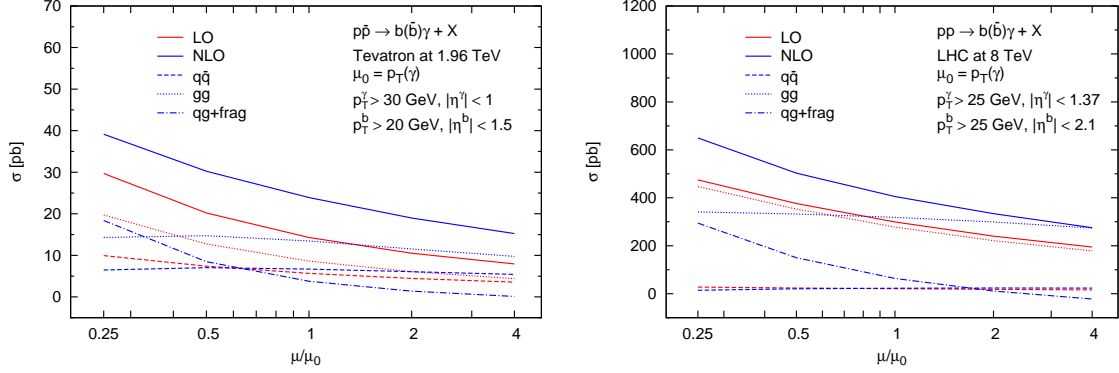


FIG. 12: Dependence of the LO (red) and NLO (blue) cross section for $pp \rightarrow b(\bar{b})\gamma + X$ (at least one b jet identified in the final state) on the renormalization/factorization scale at the Tevatron with $\sqrt{s} = 1.96$ TeV (left) and at the LHC with $\sqrt{s} = 8$ TeV (right). Both the total cross section (solid) and the contributions of the individual subprocesses, $q\bar{q}$ (dashed), gg (dotted), and qg (dash-dotted) are shown.

and illustrate the comparison between the two choices in the case of the $p_T(\gamma)$ distribution.

The scale dependence of the total cross section for the Tevatron and the LHC is shown in Fig. 12, where the contributions of the individual subprocesses are also given. Similar to the $2b$ -tag case, also in the $1b$ -tag case the impact of NLO QCD corrections is substantial and the corresponding K -factors range from 1.3 to 1.9 at the Tevatron and from 1.3 to 1.4 at the LHC, when both renormalization and factorization scales are varied in the $\mu_0/4 < \mu_R = \mu_F < 4\mu_0$ interval (for $\mu_0 = p_T(\gamma)$). The improvement of the scale dependence is also not significant when we go from LO to NLO and the residual scale dependence at NLO is also due to the qg channel, while the scale dependence of the $q\bar{q}$ and gg channels are greatly improved when the NLO QCD corrections are included, as shown in Fig. 12.

We notice that the leading subprocesses in the total cross section are now gg and qg at both at the Tevatron and the LHC. However, as we will see in Fig. 17, this is true at the level of distributions only for the LHC, while at the Tevatron the $q\bar{q}$ subprocesses still dominates at medium and large $p_T(\gamma)$ and $p_T(b)$. This will be important to understand the comparison between FFS/4FNS and VFS/5FNS that we will discuss in Sec. IIID.

In Figs. 13 and 14 we show the photon and the b -jet transverse-momentum distribution, the photon pseudorapidity and the photon-to- b -jet separation distributions at the Tevatron.

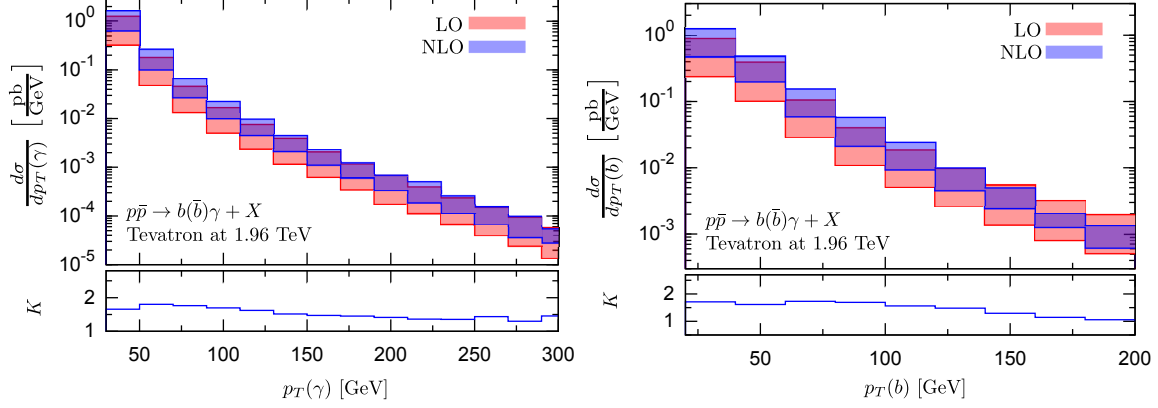


FIG. 13: The upper plots show the transverse-momentum distributions of the photon (left) and the b jet (right) for $p\bar{p} \rightarrow b(\bar{b})\gamma + X$ (at least one b jet identified in the final state) at the Tevatron with $\sqrt{s} = 1.96$ TeV. The bands correspond to the variation of the renormalization and factorization scales in the interval $\mu_0/4 < \mu < 4\mu_0$. The lower plots show the bin-by-bin K -factor for the corresponding distributions.

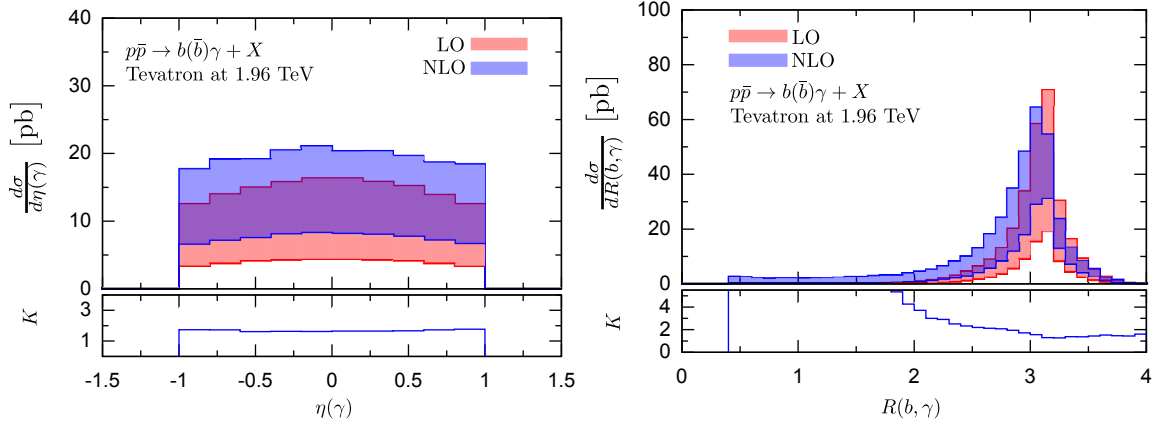


FIG. 14: The upper plots show the pseudorapidity distribution of the photon (left) and the separation between the b jet and the photon (right) for $p\bar{p} \rightarrow b(\bar{b})\gamma + X$ (at least one b jet identified in the final state) at the Tevatron with $\sqrt{s} = 1.96$ TeV. The bands correspond to the variation of the renormalization and factorization scales in the interval $\mu_0/4 < \mu < 4\mu_0$. The lower plots show the bin-by-bin K -factor for the corresponding distributions.

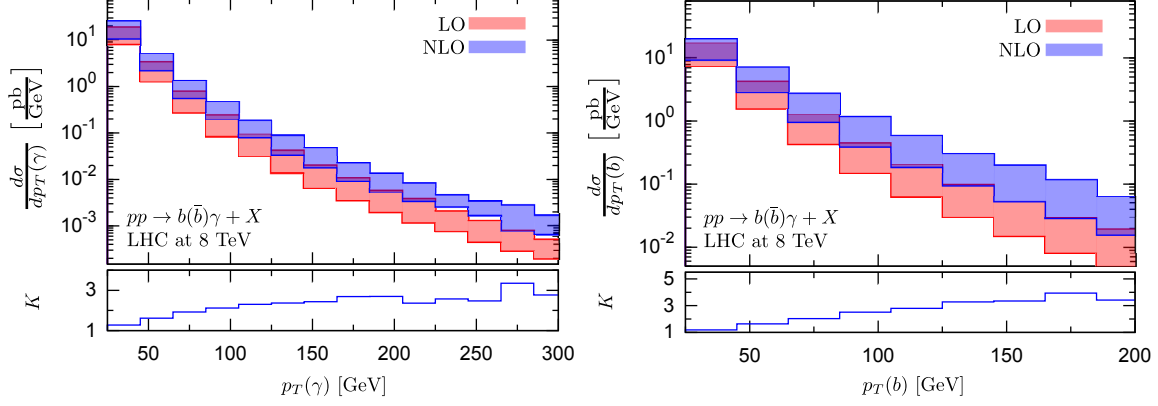


FIG. 15: The upper plots show the transverse-momentum distributions of the photon (left) and the b jet (right) for $pp \rightarrow b(\bar{b})\gamma + X$ (at least one b jet identified in the final state) at the LHC with $\sqrt{s} = 8$ TeV. The bands correspond to the variation of the renormalization and factorization scales in the interval $\mu_0/4 < \mu < 4\mu_0$. The lower plots show the bin-by-bin K -factor for the corresponding distributions.

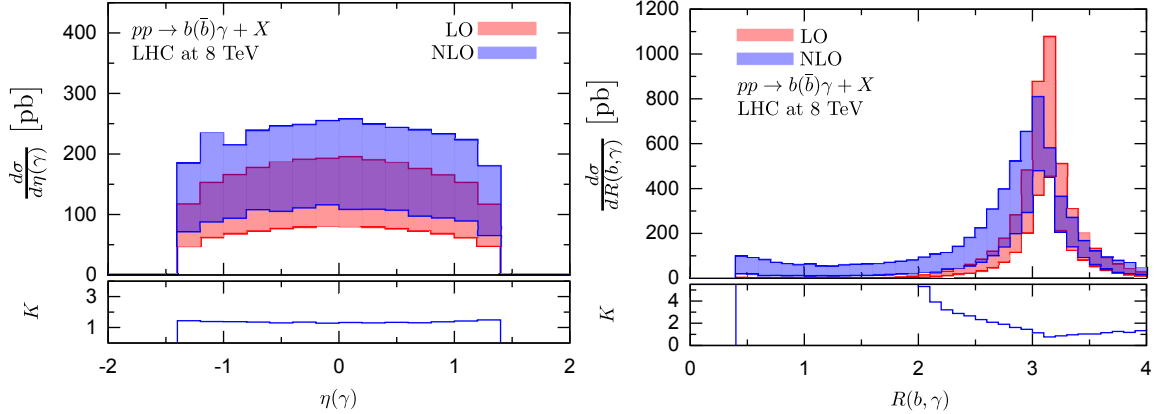


FIG. 16: The upper plots show the pseudorapidity distribution of the photon (left) and the separation between the b jet and the photon (right) for $pp \rightarrow b(\bar{b})\gamma + X$ (at least one b jet identified in the final state) at the LHC with $\sqrt{s} = 8$ TeV. The bands correspond to the variation of the renormalization and factorization scales in the interval $\mu_0/4 < \mu < 4\mu_0$. The lower plots show the bin-by-bin K -factor for the corresponding distributions.

As for the $2b$ -jet case, the bands in each figure represent the variation of the differential cross section (bin-by-bin) when the renormalization and factorization scales ($\mu_R = \mu_F$) are varied in the range $\mu_0/4 \leq \mu \leq 4\mu_0$, with $\mu_0 = p_T(\gamma)$, and the lower window of each figure

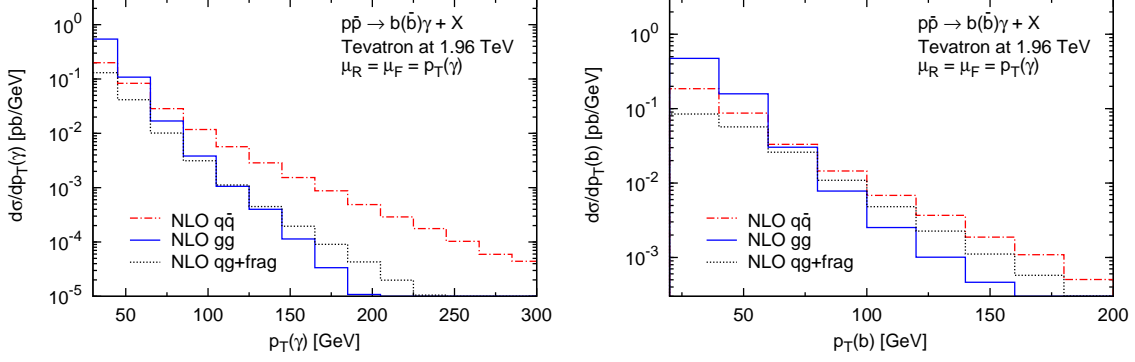


FIG. 17: Individual contributions of the $q\bar{q}$ (red), gg (blue) and qg (black) subprocesses to the transverse-momentum distributions of the photon (left) and the b jet (right) for $pp \rightarrow b(\bar{b})\gamma + X$ (at least one b jet identified in the final state) at the Tevatron with $\sqrt{s} = 1.96$ TeV, and $\mu_R = \mu_F = p_T(\gamma)$.

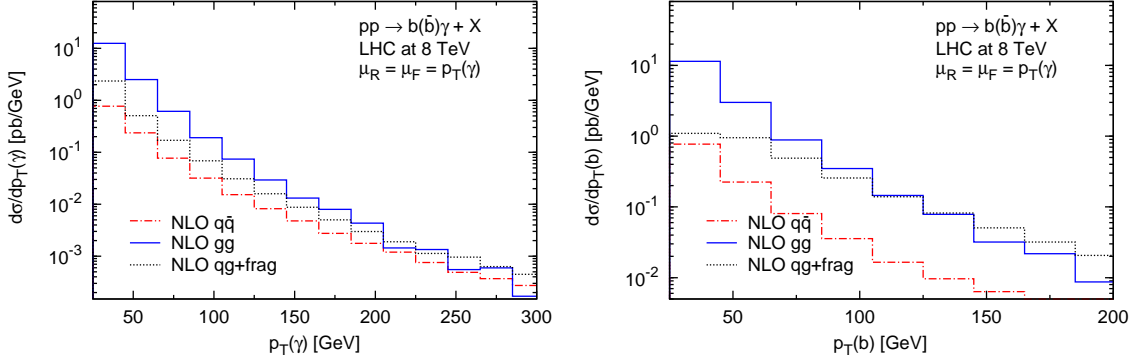


FIG. 18: Individual contributions of the $q\bar{q}$ (red), gg (blue) and qg (black) subprocesses to the transverse-momentum distributions of the photon (left) and the b jet (right) for $pp \rightarrow b(\bar{b})\gamma + X$ (at least one b jet identified in the final state) at the LHC with $\sqrt{s} = 8$ TeV, and $\mu_R = \mu_F = p_T(\gamma)$.

gives the bin-by-bin K -factor. At the Tevatron, the K -factor for both the $p_T(\gamma)$ and $p_T(b)$ distributions decreases as we go from the low- to the high- p_T region, similar to what we observed in the $2b$ -tag case. In Figs. 15 and 16 analogous plots are presented for the LHC. The impact of NLO QCD corrections to the differential distributions are quite significant. Similar to the $2b$ -tag case, the K -factor for the $p_T(\gamma)$ and $p_T(b)$ distributions grows as p_T increases. The $R(\gamma, b)$ distribution, however, does not exhibit the pinching that is present in the $2b$ -tag case.

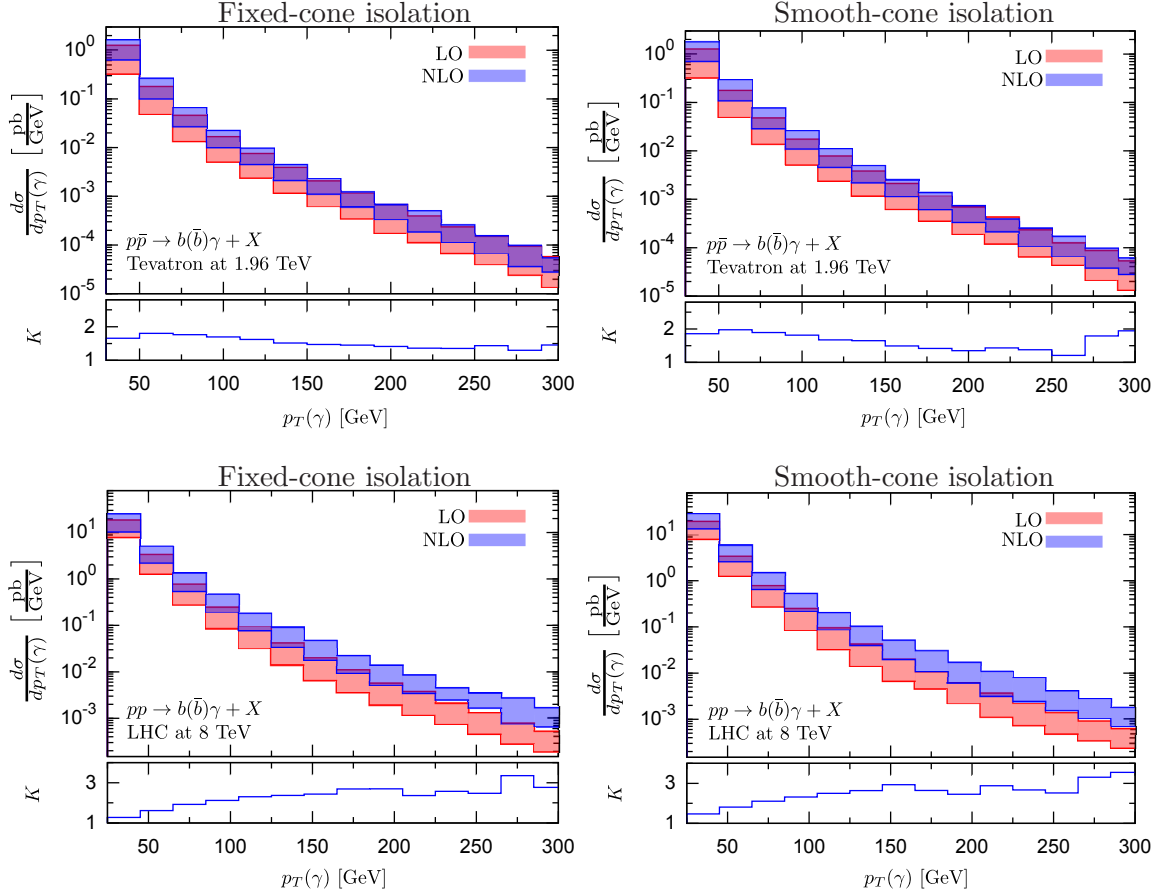


FIG. 19: Transverse-momentum distributions of the photon in $p\bar{p} \rightarrow b(\bar{b})\gamma + X$ (at least one b jet identified in the final state) at the Tevatron with $\sqrt{s} = 1.96$ TeV (top) and the LHC with $\sqrt{s} = 8$ TeV (bottom), obtained using a fixed-cone (left) or a smooth-cone (right) isolation for the hard photon. The right hand side plots are the same shown in Fig. 13 (Tevatron) and in Fig. 15 (LHC) and they are repeated here for comparison at a glance. The bands correspond to the variation of the renormalization and factorization scales in the interval $\mu_0/4 < \mu < 4\mu_0$. The lower plots show the bin-by-bin K -factor for the corresponding distributions.

In Figs. 17 and 18, the contribution of the $q\bar{q}$, gg , and qg channels to the NLO distributions are shown, allowing us to argue that the strong scale dependence in the $p_T(\gamma)$ and $p_T(b)$ distributions at the LHC are due to the qg channel that contributes significantly, almost as much as the gg channel. On the other hand, at the Tevatron the scale dependence in the distributions shows quite an improvement as $p_T(\gamma)$ or $p_T(b)$ grows, due to the $q\bar{q}$ channel that dominates in the intermediate- to high- p_T regions.

Finally, in Figs. 19 we show the comparison between using a smooth-cone or fixed-cone isolation algorithm for the hard photon. For the smooth-cone isolation prescription, we use $R_0 = 0.4$ and $\epsilon = 1$ (see Eq. 4). We illustrate it both for the Tevatron and the LHC in the case of the photon transverse-momentum distribution. The difference is visible but small at the Tevatron and very small at the LHC.

D. Comparison between 5FNS and 4FNS calculations

In Sec. IIB, we have discussed that the predictions for direct photon production in association with a bottom quark at hadron colliders, $pp(p\bar{p}) \rightarrow \gamma + b + X$, can be obtained from two different schemes. The first one is the FFS/4FNS (4FNS in the following), where there is no initial-state bottom quark in the partonic subprocesses and the mass of the bottom quark is retained in the calculation. This is essentially the $b\bar{b}\gamma$ calculation with at least one b jet tagged in the final state, whose results have been presented in the Sec. IIIC. The second scheme is the VFS/5FNS (5FNS in the following), where the bottom quark is treated as massless and can be present in the initial state of all contributing subprocesses. In this last scheme, the large logarithms that appear due to the phase-space integration of the unobserved final-state b quark (only one b quark is tagged) is resummed and absorbed into the bottom-quark PDF. The calculation of $pp(p\bar{p}) \rightarrow \gamma + b + X$ in the 5FNS has been reported in [5], where a fixed-cone isolation is used for the hard photon and the fragmentation component is included up to $\mathcal{O}(\alpha\alpha_s^2)$.

In this Section, we would like to compare the results for $pp(p\bar{p}) \rightarrow \gamma + b + X$ from the two schemes at NLO QCD accuracy. In the comparison the same hard-photon isolation prescription have to be adopted. For this reason we have reproduced the 5FNS calculation (details of which are given in Sec. IIB) using both a smooth-cone and a fixed-cone isolation prescription. This last step has allowed us to compare with Ref. [5] and has also given us more flexibility in the comparison with experimental data.

The one-loop amplitude for the $gb \rightarrow \gamma b$ subprocess is taken from Ref. [33], as implemented in the MCFM [28] code. The real corrections are computed using the two-cutoff phase-space slicing method to extract the soft and collinear singularities. The virtual+soft contribution to the $gb \rightarrow \gamma b$ subprocess also agrees with the result presented in Ref. [34]. We have compared our 5FNS calculation with the smooth-cone isolation prescription against a

modified MCFM code. Our $\gamma + b + X$ implementation in MCFM is based on the calculation of direct photon production at hadron colliders, $pp(p\bar{p}) \rightarrow \gamma + \text{jet} + X$, modified by selecting the partonic channels that are listed in Table II B with the addition of imposing the suitable b -jet selection criteria. We have cross-checked our fixed-cone isolation results with the Authors of Ref. [5] and found consistency. The only difference with respect to Ref. [5] is that we include $\mathcal{O}(\alpha\alpha_s)$ instead of $\mathcal{O}(\alpha\alpha_s^2)$ fragmentation contributions, which can be argued to be indeed consistent with the NLO QCD calculation and it is in any case expected to make a minor difference since the whole point of the isolation procedure is to reduce the impact of contributions from parton fragmentation (see our discussion in Sec. II C).

In Figs. 21 and 20 we show the comparison between the 4FNS and 5FNS calculations for the photon and the b -jet transverse-momentum distributions at the Tevatron and at the LHC, using a fixed-cone isolation prescription. The comparison using a smooth-cone isolation prescription leads to very similar results. From the plots one can see that both at the Tevatron and at the LHC the 4FNS predictions lead the 5FNS ones, but they are overall compatible within their theoretical systematic uncertainty which we base only on the renormalization and factorization scale uncertainty. This is indeed what is expected from a relatively well-behaved QCD perturbative series. It also indicates that the process under consideration is moderately sensitive to the kind of kinematic logarithms that are resummed in the b -quark PDF.

It is however interesting to understand the behavior of the scale-variation band, which is indeed different for the Tevatron and the LHC. At the LHC the distributions from the 5FNS calculation have smaller scale-uncertainty bands compared to the 4FNS counterparts. As it has been discussed in [5], at the LHC, the dominant contribution to the $p_T(\gamma)$ distribution comes from the $Qg \rightarrow \gamma Q$, $gg \rightarrow \gamma b\bar{b}$, and $Qg \rightarrow \gamma Qg$ channels (see Table II B), where potentially large kinematic logarithms have been resummed in the b -quark PDF, resulting in the better scale-dependence behavior. On the other hand, at the Tevatron, while the scale-variation bands from the 5FNS calculation are smaller than the 4FNS calculation at low $p_T(\gamma)$, as $p_T(\gamma)$ increases the 5FNS bands are getting larger, while the 4FNS bands get sensibly smaller. As we have seen in Fig. 17, the $q\bar{q} \rightarrow b\bar{b}\gamma$ channel dominates in the intermediate- to high- p_T region, and since this piece of the calculation enters in the 5FNS real correction as a tree level process, it still has a strong scale dependence.

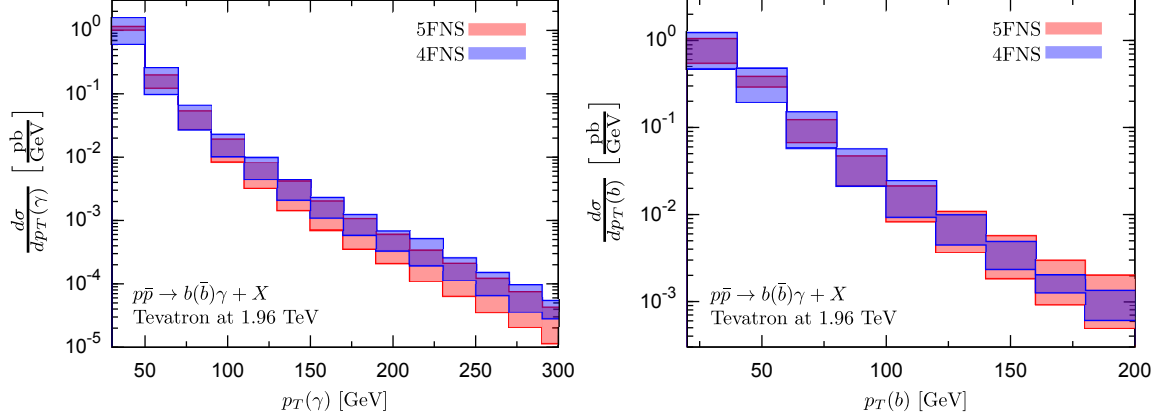


FIG. 20: Transverse-momentum distributions of the photon (left) and the b jet (right) for $p\bar{p} \rightarrow \gamma + b + X$ (at least one b jet identified in the final state) at the Tevatron with $\sqrt{s} = 1.96$ TeV, obtained from the 4FNS (blue) and the 5FNS (red) calculations. The bands correspond to the variation of the renormalization and factorization scales in the interval $\mu_0/4 < \mu < 4\mu_0$.

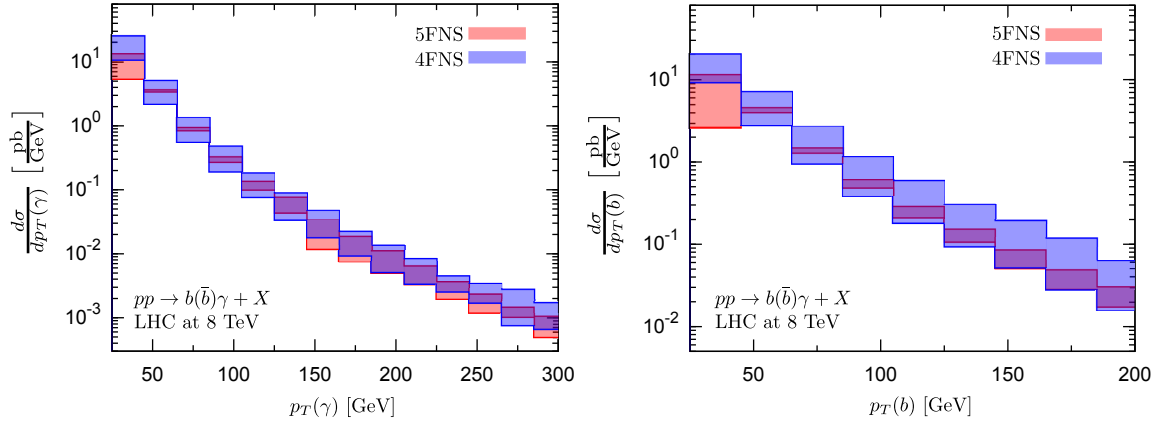


FIG. 21: Transverse-momentum distributions of the photon (left) and the b jet (right) for $pp \rightarrow \gamma + b + X$ (at least one b jet identified in the final state) at the LHC with $\sqrt{s} = 8$ TeV, obtained from the 4FNS (blue) and the 5FNS (red) calculations. The bands correspond to the variation of the renormalization and factorization scales in the interval $\mu_0/4 < \mu < 4\mu_0$.

E. Comparison of NLO QCD predictions for $\gamma + b + X$ with Tevatron data

The calculation of $b\bar{b}\gamma$ production at NLO QCD accuracy allows us to improve the theoretical prediction of the $pp(p\bar{p}) \rightarrow \gamma + b + X$ process at hadron colliders and to compare with the recent measurements of direct-photon production with at least one b jet ($\gamma + b + X$) at

the Tevatron by the CDF [9] and D0 [7] collaborations.

Since the measurement of the $\gamma + b + X$ process at the Tevatron employed the fixed-cone photon isolation we will specify both 4FNS and 5FNS to this prescription and adopt otherwise the identification cuts used by CDF [9],

$$\begin{aligned} p_T(\gamma) &> 30 \text{ GeV}, |\eta(\gamma)| < 1, \\ \text{Photon isolation: } R_0 &= 0.4, E_T^{\text{max}} = 2 \text{ GeV}, \\ p_T(b, j) &> 20 \text{ GeV}, |\eta(b, j)| < 1.5, R = 0.4, \end{aligned}$$

and D0 [7],

$$\begin{aligned} p_T(\gamma) &> 30 \text{ GeV}, |\eta(\gamma)| < 1 \quad \text{and} \quad 1.5 < |\eta(\gamma)| < 2.5, \\ \text{Photon isolation: } R_0 &= 0.4, E_T^{\text{max}} = 2.5 \text{ GeV}, \\ p_T(b, j) &> 15 \text{ GeV}, |\eta(b, j)| < 1.5, R = 0.5, \end{aligned}$$

when comparing with each experiment respectively. From the detailed tables given by both CDF [9] and D0 [7] in their papers we have been able to provide a comparison between the experimental data, the 5FNS NLO predictions of Ref. [5], and our 4FNS NLO predictions, including the corresponding statistical and systematic uncertainties.

Since the results of Ref. [5] used CTEQ6.6 as PDF set, and estimate the systematic theoretical uncertainty from renormalization- and factorization-scale dependence by varying them in the $\mu_0/2 < \mu_R = \mu_F < 2\mu_0$ range ($\mu_0 = p_T(\gamma)$), we ought to specify our results to this set-up to have a more adequate comparison⁴. At the same time, we think that it is important to have a comparison using a more up-to-date set of PDFs, such as the CT10nlo_nf4 set that we use in the rest of this paper. We also consider the variation of μ_R and μ_F in the $\mu_0/4 < \mu_R = \mu_F < 4\mu_0$ range a more accurate representation of the theoretical uncertainty of our predictions, given what has been discussed in Sec. III C. Therefore, for each experiment we will present a comparison using the same setup (CTEQ6.6 and $\mu_0/2 < \mu_R = \mu_F < 2\mu_0$) for both 5FNS and 4FNS NLO results, and a comparison where the 5FNS results are the same but the 4FNS results use updated PDFs and a more realistic systematic uncertainty (CT10nlo_nf4 and $\mu_0/4 < \mu_R = \mu_F < 4\mu_0$).

⁴ For the case of the comparison with D0 in the forward region we only plot 5FNS for $\mu = \mu_0$ because we were not provided the full scale variation. We decided not to reproduce the band ourselves because the results of Ref. [5], to which the experiments have compared in their papers, include fragmentation contributions at $O(\alpha_s^2)$ while we only include them at $O(\alpha_s)$. These effects are small, but we prefer to show a consistent set of 5FNS results.

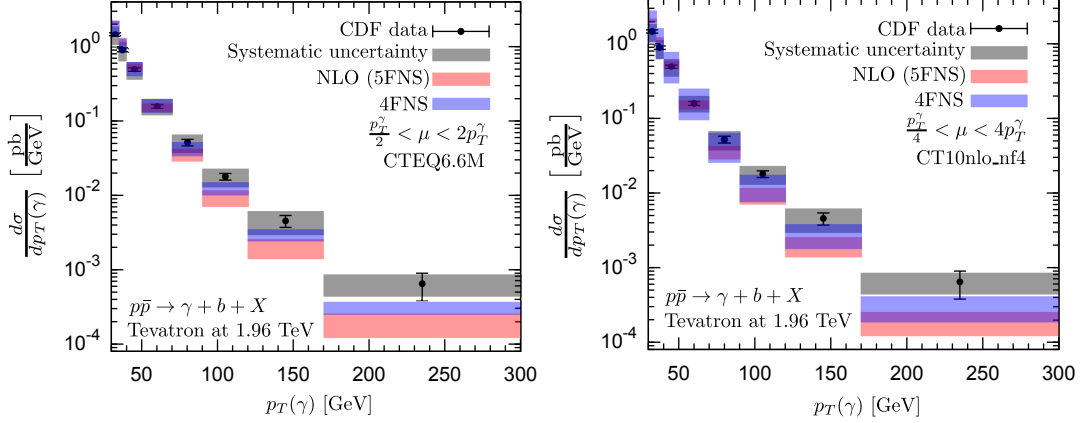


FIG. 22: The photon- p_T distribution for $\gamma + b + X$ at the Tevatron with $\sqrt{s} = 1.96$ TeV and the identification cuts used by the CDF experiment. The numbers for the CDF data and the NLO 5FNS calculation (red) [5] are taken from [9]. The NLO 4FNS results (blue) are from this paper. For the experimental data, the gray band represent the systematic uncertainty only, while both systematic and statistic uncertainties are included in the error bars. The 5FNS NLO results have been obtained using CTEQ6.6 PDFs and the systematic uncertainty band corresponds to varying μ_R and μ_F in the $\mu_0/2 < \mu_R = \mu_F < 2\mu_0$ range. The 4FNS results have been obtained using the same set-up (left) as well as using CT10nlo_nf4 PDFs and varying μ_R and μ_F in the $\mu_0/4 < \mu_R = \mu_F < 4\mu_0$ range (right).

The results are presented in Figs. 22 and 23 for CDF and D0 respectively. We notice that the 4FNS NLO results show a better agreement with data in the high $p_T(\gamma)$ region. This is not surprising since it is mainly induced by the fact that at the Tevatron $q\bar{q} \rightarrow b\bar{b}\gamma$ is the leading subprocess in the high- $p_T(\gamma)$ region and this channel is only included at tree level in the 5FNS calculation, while it is enhanced by NLO corrections in the 4FNS calculation.

IV. CONCLUSIONS

In this paper we have reported the NLO QCD calculation of hard-photon production with heavy quarks at hadron colliders ($pp(p\bar{p}) \rightarrow Q\bar{Q}\gamma$ with $Q = t, b$), and we have provided results for $\gamma + 2b$ - and $\gamma + 1b$ -jet production at both the Tevatron with center-of-mass energy 1.96 TeV and the Large Hadron Collider with center-of-mass energy 8 TeV. We have compared with the CDF and D0 measurements of hard-photon production with at least

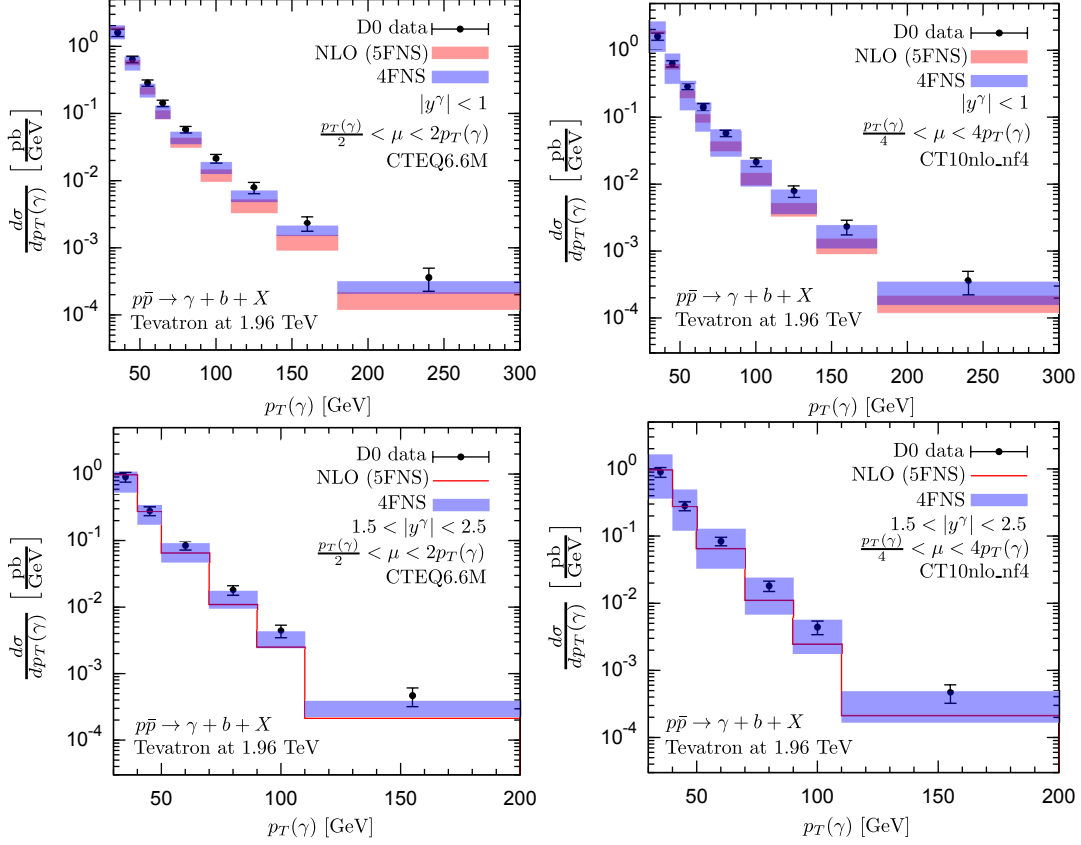


FIG. 23: The photon- p_T distribution for $\gamma + b + X$ at the Tevatron with $\sqrt{s} = 1.96$ TeV and the identification cuts used by the D0 experiment. The numbers for the CDF data and the NLO 5FNS calculation (red) [5] are taken from [7]. The NLO 4FNS results (blue) are from this paper. For the experimental data, we have considered both the central- and the forward-rapidity data. Both systematic and statistic uncertainties are included in the error bars. The 5FNS NLO results have been obtained using CTEQ6.6 PDFs and uncertainty band corresponds to varying μ_R and μ_F in the $\mu_0/2 < \mu_R = \mu_F < 2\mu_0$ range. For the forward-rapidity region only the central values were available. The 4FNS results have been obtained using the same set-up (left) as well as using CT10nlo_nf4 PDFs and varying μ_R and μ_F in the $\mu_0/4 < \mu_R = \mu_F < 4\mu_0$ range (right).

one b jet [7, 9] and found consistency. Future results for $\gamma + 1b$ - and $\gamma + 2b$ -jet production from ATLAS and CMS will offer the opportunity to test the NLO QCD prediction for these processes in different energy and kinematic regimes. Future studies could also make use of the existing implementation of our calculation in a full-fledged NLO parton-shower Monte Carlo (e.g. Sherpa).

The level of uncertainty in the theoretical predictions is adequate to compare with current experimental accuracies, and offer the first opportunity to constrain the b -quark parton distribution function.

Finally, a non trivial extension of our calculation could involve considering the production of a hard photon with charm quarks to be used as a direct probe of the charm-quark parton distribution function.

Acknowledgements

H. B. H. and L. R. would like to greatly thank Tzvetalina Stavreva for her help in comparing with the results of Ref. [5], Stefan Hoeche for his help in implementing the NLO calculation of $Q\bar{Q}\gamma$ into the Sherpa Monte Carlo event generator, Ciaran Williams and Nobuo Sato for useful discussions. L. R. would like to thank the Aspen Center for Physics for its kind hospitality while part of this work was being completed. The work of H. B. H. and L. R. is supported in part by the U.S. Department of Energy under grants DE-FG02-13ER41942.

-
- [1] U. Baur, A. Juste, L. Orr, and D. Rainwater, Phys.Rev. **D71**, 054013 (2005), hep-ph/0412021.
 - [2] U. Baur, A. Juste, L. Orr, and D. Rainwater, Nucl.Phys.Proc.Suppl. **160**, 17 (2006), hep-ph/0606264.
 - [3] P.-F. Duan, W.-G. Ma, R.-Y. Zhang, L. Han, L. Guo, et al., Phys.Rev. **D80**, 014022 (2009).
 - [4] K. Melnikov, M. Schulze, and A. Scharf, Phys.Rev. **D83**, 074013 (2011), 1102.1967.
 - [5] T. Stavreva and J. Owens, Phys.Rev. **D79**, 054017 (2009), 0901.3791.
 - [6] V. Abazov et al. (D0 Collaboration), Phys.Rev.Lett. **102**, 192002 (2009), 0901.0739.
 - [7] V. Abazov et al. (D0 Collaboration), Phys.Lett. **B714**, 32 (2012), 1203.5865.
 - [8] T. Aaltonen et al. (CDF Collaboration), Phys.Rev. **D81**, 052006 (2010), 0912.3453.
 - [9] T. Aaltonen et al. (CDF Collaboration) (2013), 1303.6136.
 - [10] T. Sjostrand, S. Mrenna, and P. Z. Skands, JHEP **0605**, 026 (2006), hep-ph/0603175.
 - [11] T. Sjostrand, S. Mrenna, and P. Z. Skands, Comput.Phys.Commun. **178**, 852 (2008), 0710.3820.

- [12] T. Gleisberg, S. Hoeche, F. Krauss, A. Schalicke, S. Schumann, et al., JHEP **0402**, 056 (2004), hep-ph/0311263.
- [13] T. Gleisberg, S. Hoeche, F. Krauss, M. Schonherr, S. Schumann, et al., JHEP **0902**, 007 (2009), 0811.4622.
- [14] A. Lipatov, M. Malyshev, and N. Zotov, JHEP **1205**, 104 (2012), 1204.3828.
- [15] V. Hirschi, R. Frederix, S. Frixione, M. V. Garzelli, F. Maltoni, et al., JHEP **1105**, 044 (2011), 1103.0621.
- [16] H. B. Hartanto, Ph.D. thesis, Florida State University (2013).
- [17] L. Reina and T. Schutzmeier, JHEP **1209**, 119 (2012), 1110.4438.
- [18] J. Vermaseren (2000), math-ph/0010025.
- [19] G. Passarino and M. Veltman, Nucl.Phys. **B160**, 151 (1979).
- [20] A. Denner and S. Dittmaier, Nucl.Phys. **B734**, 62 (2006), hep-ph/0509141.
- [21] T. Diakonidis, J. Fleischer, J. Gluza, K. Kajda, T. Riemann, et al., Phys.Rev. **D80**, 036003 (2009), 0812.2134.
- [22] R. K. Ellis and G. Zanderighi, JHEP **0802**, 002 (2008), 0712.1851.
- [23] S. Catani and M. Seymour, Nucl.Phys. **B485**, 291 (1997), hep-ph/9605323.
- [24] S. Catani, S. Dittmaier, M. H. Seymour, and Z. Trocsanyi, Nucl.Phys. **B627**, 189 (2002), hep-ph/0201036.
- [25] L. Bourhis, M. Fontannaz, and J. P. Guillet, Eur. Phys. J. **C2**, 529 (1998), hep-ph/9704447.
- [26] A. Gehrmann-De Ridder and E. N. Glover, Eur.Phys.J. **C7**, 29 (1999), hep-ph/9806316.
- [27] S. Frixione, Phys.Lett. **B429**, 369 (1998), hep-ph/9801442.
- [28] J. M. Campbell and R. K. Ellis, Nucl.Phys.Proc.Suppl. **205-206**, 10 (2010), 1007.3492.
- [29] J. Pumplin, D. Stump, J. Huston, H. Lai, P. M. Nadolsky, et al., JHEP **0207**, 012 (2002), hep-ph/0201195.
- [30] H.-L. Lai, M. Guzzi, J. Huston, Z. Li, P. M. Nadolsky, et al., Phys.Rev. **D82**, 074024 (2010), 1007.2241.
- [31] G. Aad et al. (ATLAS Collaboration), Phys.Rev. **D85**, 092014 (2012), 1203.3161.
- [32] G. Aad et al. (ATLAS Collaboration), JHEP **1306**, 084 (2013), 1302.2929.
- [33] P. Aurenche, R. Baier, A. Douiri, M. Fontannaz, and D. Schiff, Nucl.Phys. **B286**, 553 (1987).
- [34] H. Baer, J. Ohnemus, and J. Owens, Phys.Rev. **D42**, 61 (1990).